HEP'99 # 1_144
Submitted to Pa 1
Pl 1

DELPHI 99-114 CONF 301
15 June 1999

QCD Results from the Measurements of Event Shape Distributions between 41 GeV and 189 GeV

Preliminary

DELPHI Collaboration

Paper submitted to the HEP'99 Conference
Tampere, Finland, July 15-21

DELPHI Collaboration DELPHI 99-114 CONF 301
15 June 1999

QCD Results from the DELPHI Measurements of Event Shape and Inclusive Particle Distributions between 41 GeV and 189 GeV

J.Drees, U.Flagmeyer, K.Hamacher, O.Passon, R.Reinhardt and D.Wicke
Fachbereich Physik, Bergische Universität-GH Wuppertal
Gaußstraße 20, 42097 Wuppertal, Germany

Abstract

Jet rates, infrared and collinear safe event shape distributions and their mean values are determined at various centre-of-mass energies between 41 GeV and 189 GeV using the data taken with the DELPHI detector at LEP. Data above 91 GeV taken from the high energy run of LEP and data below 91 GeV selected by tagging events with prompt photon radiation are used for the analysis. From the event shapes, the strong coupling α_s is extracted in $\mathcal{O}(\alpha_s^2)$ and in NLLA. Hadronisation corrections evaluated with fragmentation model generators as well as an analytical power ansatz are applied. Comparing these measurements to those obtained at and around M_{Z}, the energy dependence (running) of α_s is accessible.

Conference contribution for TAMPERE 1999

1 Introduction

This note is related to the paper "α_s from DELPHI Measurements at LEP 2", (accepted by Phys. Letters B) [1] The analysis described [1] is repeated and extended to the 1998 energy run at 189 GeV and to energies below M_Z. The event shapes, their means and moments and the results of α_s at energies between 91 GeV and 183 GeV are taken from [1].

In 1998 LEP operated at a centre-of-mass energy of 189 GeV. Event shape distributions and jet rates are measured and compared to the results from previous measurements[1] at centre-of-mass energies between 133 GeV and 183 GeV. The statistics of hadronic events collected at these energies, though small compared to the statistics gathered near the Z resonance, is sufficient for the measurement of event shape distributions and for a determination of the strong coupling α_s. To obtain the running of α_s the data taken around 91.2 GeV in 1993–95 were reanalyzed using cuts, binnings and fit ranges coherent with the high energy data analysis. These cuts have been optimized for a consistent measurement of the running of α_s over a wide range of energies, and do not achieve the best possible results for Z Data. For a precision measurement of α_s from Z data see [22]

Further improvements in the determination of the running of α_s arise from the analysis of QCD events at centre-of-mass energies below 91 GeV arising from prompt photon radiation (ISR, FSR), selected by using a photon tagging technique. The Z data collected in 1992–95 is used for the selection of low energy event samples.

The statistics obtained at reduced centre-of-mass energies of 41 GeV, 65 GeV, and 77 GeV is comparable to that collected in the high energy run and sufficient for the measurement of event shape distributions and for a determination of the strong coupling α_s.

In section 2 the selection of hadronic events, the reconstruction of the centre-of-mass energy, the correction procedures applied to the data, and for energies above the WW threshold the suppression of $\mathrm{W^+W^-}$ events are briefly discussed. Section 3 gives an overview about the selection of hadronic events with centre-of-mass energies below M_Z. Section 4 presents event shapes and jet rates and the comparison of the data with predictions from $q\bar{q}$-based hadronic generators. In section 5, measurements of α_s and the running of α_s, using various techniques, are presented.

2 Selection and Correction of Hadronic Data

The analysis is based on data taken with the DELPHI detector at seven different centre-of-mass energies between 91 GeV and 189 GeV. The results for 91.2 GeV are obtained using 1993 to 1995 data. The data taken at 130 GeV and 136 GeV in the years 1995 and 1997 are averaged and given as results at $E_{\mathrm{cm}} = 133$ GeV, their average centre-of-mass energy. The integrated luminosities collected at these energies are given in Table 1.

DELPHI is a hermetic detector with a solenoidal magnetic field of 1.2 T. The tracking detectors, situated in front of the electro-magnetic calorimeters are a silicon micro-vertex detector VD, a combined jet/proportional chamber inner detector ID, a time projection chamber TPC as the major tracking device, and the streamer tube detector OD in the barrel region. The forward region is covered by silicon mini-strip and pixel detectors (VFT) and by the drift chamber detectors FCA and FCB.

The electromagnetic calorimeters are the high density projection chamber HPC in the barrel, and the lead-glass calorimeter FEMC in the forward region. Detailed information about the design and performance of DELPHI can be found in [3, 4].

In order to select well measured charged particle tracks, the cuts given in the upper part of Table 2 have been applied. The cuts in the lower part of the table are used to select $e^+e^- \to \mathrm{Z}/\gamma \to q\bar{q}$ events and to suppress background processes such as two-photon interactions, beam-gas and beam-wall interactions, leptonic final states, and, for the LEP2 analysis, initial state radiation (ISR) and WW pair production (for energies above the WW threshold).

At energies above 91.2 GeV, the large cross-section of the Z resonance peak raises the possibility of hard ISR allowing the creation of a nearly on-shell Z boson. These 'radiative return events' constitute a large fraction of all hadronic events. The initial state photons are typically aligned along the beam direction and are rarely identified inside the detector. In order to evaluate the effective hadronic centre-of-mass energy of an event, considering ISR, an algorithm called SPRIME+ is used [5]. SPRIME+ is based on a fit imposing four-momentum conservation to measured jet four-momenta (including estimates of their errors). Several assumptions about the event topology are tested. The decision is taken according to the χ^2 obtained from the constrained fits with different topologies.

Figure 1(left) shows the spectra of the calculated energies for simulated and measured events passing general event cuts for the 189 GeV data from 1998. The agreement between data and simulation is reasonable for the high energies relevant to this analysis, while the peak around M_Z appears to be slightly shifted in the simulation. A cut on the reconstructed centre-of-mass energy $\sqrt{s'_\mathrm{rec}} \geq 90\% E_\mathrm{cm}$ is applied to discard radiative return events (see Table 2). Simulation shows that this cut keeps more than 96% of the events without ISR ($\sqrt{s} - \sqrt{s'} < 0.1$ GeV), giving a contamination with events having $\sqrt{s} - \sqrt{s'} > 10$ GeV of less than 15%.

Two photon and leptonic events are strongly suppressed by the cuts and were found to be negligible in this analysis.

Since the topological signatures of QCD four jet events and hadronic WW events (and other four quark backgrounds) are similar, no highly efficient separation of the two classes of events is possible. Furthermore any WW rejection implies a severe bias to the shape distributions of QCD events, which needs to be corrected with simulation. By applying a cut on an observable calculated from the narrow event hemisphere only, the bias to event

E_cm	133 GeV	161 GeV	172 GeV	183 GeV	189 GeV
$\mathcal{L}$	11.9 pb^{-1}	10.1 pb^{-1}	10.0 pb^{-1}	54 pb^{-1}	157.4 pb^{-1}
$\sigma_{q\bar{q}}$	292 pb	147 pb	121.0 pb	100.3 pb	99.8 pb
$\sigma_{q\bar{q}\ (\sqrt{s'}>0.85\sqrt{s})}$	74 pb	35 pb	29 pb	24.5 pb	24.3 pb
σ_WW	—	3.3 pb	12.1 pb	15.4 pb	16.65 pb
No. hadronic events	846	359	289	1338	3520

Table 1: Total cross-sections $\sigma_{q\bar{q}}$ and σ_WW as used in the simulation, high energy cross-sections $\sigma_{q\bar{q}\ (\sqrt{s'}>0.85\sqrt{s})}$ as predicted by ZFITTER 5.12 [2], integrated luminosities $\mathcal{L}$, and finally selected (non-radiative) hadronic events for the various energies.

neutral Track selection	$E \geq 0.5\,\mathrm{GeV}$ $20^\circ \leq \theta \leq 160^\circ$
charged Track selection	$0.4\,\mathrm{GeV} \leq p \leq 100\,\mathrm{GeV}$ $20^\circ \leq \theta \leq 160^\circ$ $\Delta p/p \leq 1.0$ measured track length ≥ 30 cm distance to I.P in $r\phi$ plane ≤ 4 cm distance to I.P. in $z \leq 10$ cm
Event selection	$N_{\mathrm{charged}} \geq 7$ $25^\circ \leq \theta_{\mathrm{Thrust}} \leq 155^\circ$ $E_{\mathrm{tot}} \geq 50\% E_{\mathrm{cm}}$
ISR rejection	$\sqrt{s'_{\mathrm{rec}}} \geq 90\% E_{\mathrm{cm}}$
WW rejection ($E_{\mathrm{cm}} \geq 161\,\mathrm{GeV}$)	$N_{\mathrm{charged}} \leq 42$ $B_{\mathrm{min}} \leq 0.08$

Table 2: Selection of tracks and events. p is the momentum, Δp its error, r the radial distance to the beam-axis, z the distance to the beam interaction point (I.P.) along the beam-axis, ϕ the azimuthal angle, N_{charged} the number of charged particles, θ_{Thrust} the polar angle of the thrust axis with respect to the beam, E_{tot} the total energy carried by all particles, $\sqrt{s'_{\mathrm{rec}}}$ the reconstructed centre-of-mass energy, $E_{\mathrm{cm}} = \sqrt{s}$ the nominal centre-of-mass energy, and B_{min} is the narrow jet broadening.

shape observables mainly sensitive to the wide event hemisphere is reduced. To separate $q\bar{q}$ from WW events, the shape B_{min} (as defined in [7]) is chosen. The discrimination due to B_{min} is demonstrated in Figure 1(right) for the 189 GeV data.

The remaining WW and ZZ contributions are estimated by Monte Carlo generators and subtracted from the measurement. The simulations are normalized using the cross-sections given in Table 1. The quoted σ_{WW} values correspond to a W mass of 80.35 GeV.

The remaining detector and cut effects are unfolded with simulation. The influence of detector effects was studied by passing generated events (JETSET/PYTHIA [6] using the DELPHI tuning described in [7]) through a full detector simulation (DELSIM [3]). These Monte Carlo events are processed with the reconstruction program and selection cuts as are the real data. In order to correct for cuts, detector, and ISR effects a bin by bin acceptance correction C, obtained from $e^+e^- \to \mathrm{Z}/\gamma \to q\bar{q}$ simulation, is applied to the data:

$$C_{i,\mathrm{QCD}} = \frac{h(f_i)_{\mathrm{gen,noISR}}}{h(f_i)_{\mathrm{qcdacc}}} \cdot \frac{h(f_i)_{\mathrm{qcdacc}}}{h(f_i)_{\mathrm{acc}}} \tag{1}$$

where $h(f_i)_{\mathrm{gen,noISR}}$ represents bin i of the shape distribution f generated with the tuned generator. The subscript noISR indicates that only events without a relevant Energy loss due to initial state radiation ($\sqrt{s} - \sqrt{s'} < 0.1\,\mathrm{GeV}$) enter the distribution. $h(f_i)_{\ldots\mathrm{acc}}$ represents the accepted distribution f as obtained with the full detector simulation. For $h(f_i)_{\mathrm{qcdacc}}$ all but WW cuts are applied, for $h(f_i)_{\mathrm{acc}}$ also the WW cuts are applied.

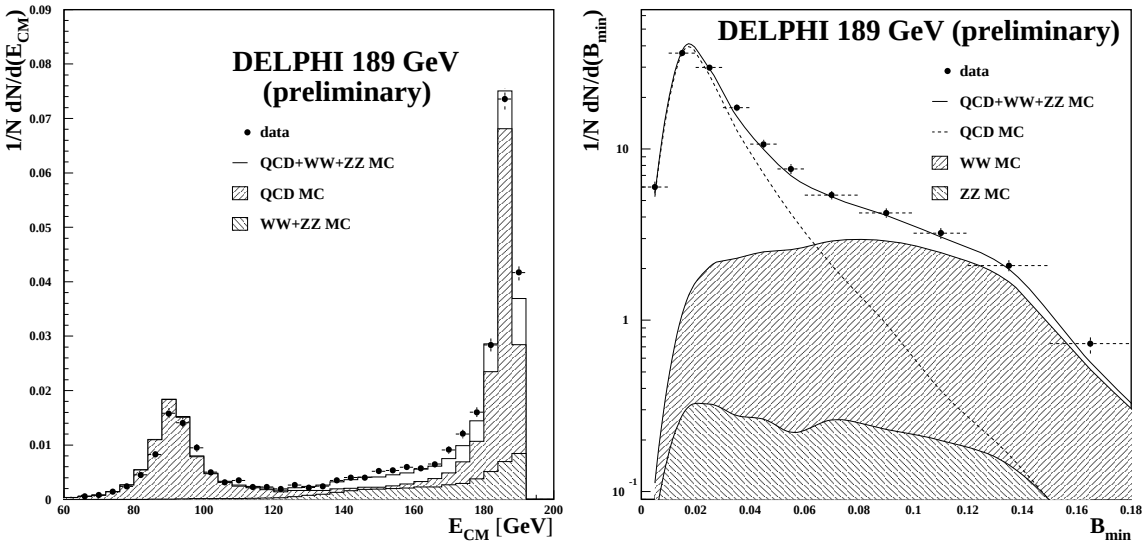

Figure 1: Left: Reconstructed centre-of-mass energy (data with $E_{\rm cm} = 189\,\mathrm{GeV}$). Right: Discriminant variables $B_{\rm min}$ for $q\bar{q}$, WW and ZZ events, $E_{\rm cm} = 189\,\mathrm{GeV}$. In both plots the simulations are based on PYTHIA [6] and DELSIM [3]. Data are shown before WW cuts and without WW subtraction, in the left plot also without ISR cut.

3 Selection of Hadronic Data with Centre-of-mass Energies below M_Z

In order to improve the sensitivity on the running of α_s events with reduced centre-of-mass energies due to hard photon radiation are selected from the 91 GeV runs of 1992–95. The approach is based on the hypothesis, that photons emitted before or immediately after the Z/γ interaction do not interfere with the QCD processes. The angular distribution of the initial state photons is aligned along the direction of the initial state particles, with the result, that most photons go undetected in the very forward region. In contrast photons from final state radiation groups along the direction of the final state partons and can be detected with better efficiency. As a result the selected events stem dominantly from final state radiation.

In order to distinguish prompt photons from soft collinear photons from the later stages of fragmentation and decays, hard cuts on the photon energy and the isolation with respect to other jets have to be applied. A two step isolation criterium is used, demanding a minimal isolation from the next jet, and a minimum energy deposition of other tracks within this angle, which reduces background from π^0 decays. An exception is made for nearby energy depositions in the HCAL which result from a leak out of the electromagnetic shower out of the HPC and are usually misidentified as neutrons. For events in the barrel region the high granularity of the HPC is exploited in order to identify photons from π^0 decays, which overlap in their energy deposition. This is done by measuring the asymmetry of the energy distribution in the $\theta\phi$-plane. The selection criteria for ISR and FSR events are summarized in Table 3.

From selected events the tagged photon is removed, and the event is boosted into the centre-of-mass frame of the hadronic system. The events are summed up into three intervals of centre-of-mass energies. The mean value of each sample is taken as the nominal energy and a correction is applied, which accounts for the differences. The number of reconstructed events, their centre-of-mass energies and the belonging purities are given in Table 4.

neutral Track selection	$E \geq 0.5\,\mathrm{GeV}$ $20^\circ \leq \theta \leq 160^\circ$
charged Track selection	$0.4\,\mathrm{GeV} \leq p \leq 100\,\mathrm{GeV}$ $\Delta p/p \leq 1.0$ measured track length ≥ 30 cm distance to I.P in $r\phi$ plane ≤ 4 cm distance to I.P. in $z \leq 10$ cm $20^\circ < \theta_{\mathrm{track}} < 160^\circ$
Standard event selection	$N_{\mathrm{charged}} \geq 7$ $30^\circ \leq \theta_{\mathrm{Thrust}} \leq 150^\circ$ $E_{\mathrm{tot}} \geq 0.50 E_{\mathrm{cm}}$
Prompt Photon selection	$4^\circ < \theta_\gamma < 176^\circ$ $E_\gamma - 10\,\mathrm{GeV} < E_W < E_\gamma + 5\,\mathrm{GeV}$ $11\,\mathrm{GeV} < p_\gamma < E_{cm}/2$ $\alpha_\gamma = 22^\circ$ $E_\alpha < 0.5\,\mathrm{GeV}$

Table 3: Selection of tracks and events for radiative events. p is the momentum, Δp its error, r the radial distance to the beam-axis, z the distance to the beam interaction point (I.P.) along the beam-axis, ϕ the azimuthal angle, N_{charged} the number of charged particles, θ_{Thrust} the polar angle of the thrust axis with respect to the beam, E_{tot} the total energy carried by all particles, θ_{track} the polar angle of the tracks with respect to the beam axis , E_γ the energy of the detected photon, E_W the angular energy, p_γ the momentum of the detected photon, α_γ the angle of its isolating cone and E_α the maximum energy within this cone.

The statistics of hadronic events collected at energies between 41 GeV and 77 GeV is comparable to those from LEP2 data and sufficient for the measurement of event shape distributions and for a determination of the strong coupling α_s.

4 Event Shapes and Jet Rates

Selected event shape distributions are shown in Figures 2–4. Figures 2 and 3 show the results from 189 GeV centre-of-mass energy, while Figure 4 shows the energy dependence

Reconstructed E_{CM}	40.9 GeV	64.8 GeV	77.3 GeV
Number of events	712	1252	1557
Purity	0.87	0.91	0.88

Table 4: Events with centre-of-mass energies below 91 GeV.

of the observables Thrust and M_{High} for energies below 91 GeV. The exact definitions of the observables used are comprehensively collected in Appendix A of [7].

The data in Figures 2–4 are corrected to be comparable with pure $e^+e^- \to \mathrm{Z}/\gamma \to q\bar{q}$ simulation of charged and neutral hadron production.The plots show a reasonable agreement between the data and Monte Carlo models.

Table 8 and Table 9 give the moments of some QCD relevant shape variables. The means and moments are calculated by integrating the fully corrected (binned) shape distributions. In order to correct for the error due to binning, a correction factor calculated as the ratio of the exact simulation result over the binned simulation result is applied. The uncertainty due to this correction is accounted for by adding 10% of this binning correction as well as 10% of the change due to the correction factor C_{QCD} to the systematic errors of the moments. In addition, contributions to the systematic error were included from changes arising from varying the ISR, WW and event cuts as well as changing the assumed WW cross-section by 5% (10% for 161 GeV). Finally the effect of replacing JETSET/PYTHIA by HERWIG 5.8d [8] as basis for the detector simulation DELSIM was investigated. Though HERWIG implements a more complete description of ISR, the resulting contribution to the systematic error is small.

For some observables the spread of the results obtained in three individual years of Z-peak data taking exceeds the estimated systematic error. In this case this spread is taken as systematic error.

Figure 5 shows the jet rates R_2, R_3, R_4 and R_5 as a function of y_{cut} as determined with the JADE, DURHAM and CAMBRIDGE jet algorithms for the 189 GeV data. The CAMBRIDGE algorithm is a modified $k_\perp$-clustering jet algorithm similar to the DURHAM algorithm. It preserves the advantages of the original DURHAM algorithm while reducing non-perturbative corrections and providing better resolution of jet substructure. A detailed description of the CAMBRIDGE algorithm can be found in [9]. Within errors, the data at all energies agree with the generator predictions tuned to Z data. No indication for a significant excess of multi-jet events is observed.

5 Determination of α_s

5.1 α_s from Event Shape Means

Event shape means $\langle f \rangle$ are determined using all hadronic events, and thus they have the advantage of minimizing the statistical error and are therefore especially well suited for low statistics analysis.

The analytical power ansatz for non-perturbative corrections by Dokshitzer and Webber [10, 11] including the Milan factor established by Dokshitzer et. al. [12, 13] is used

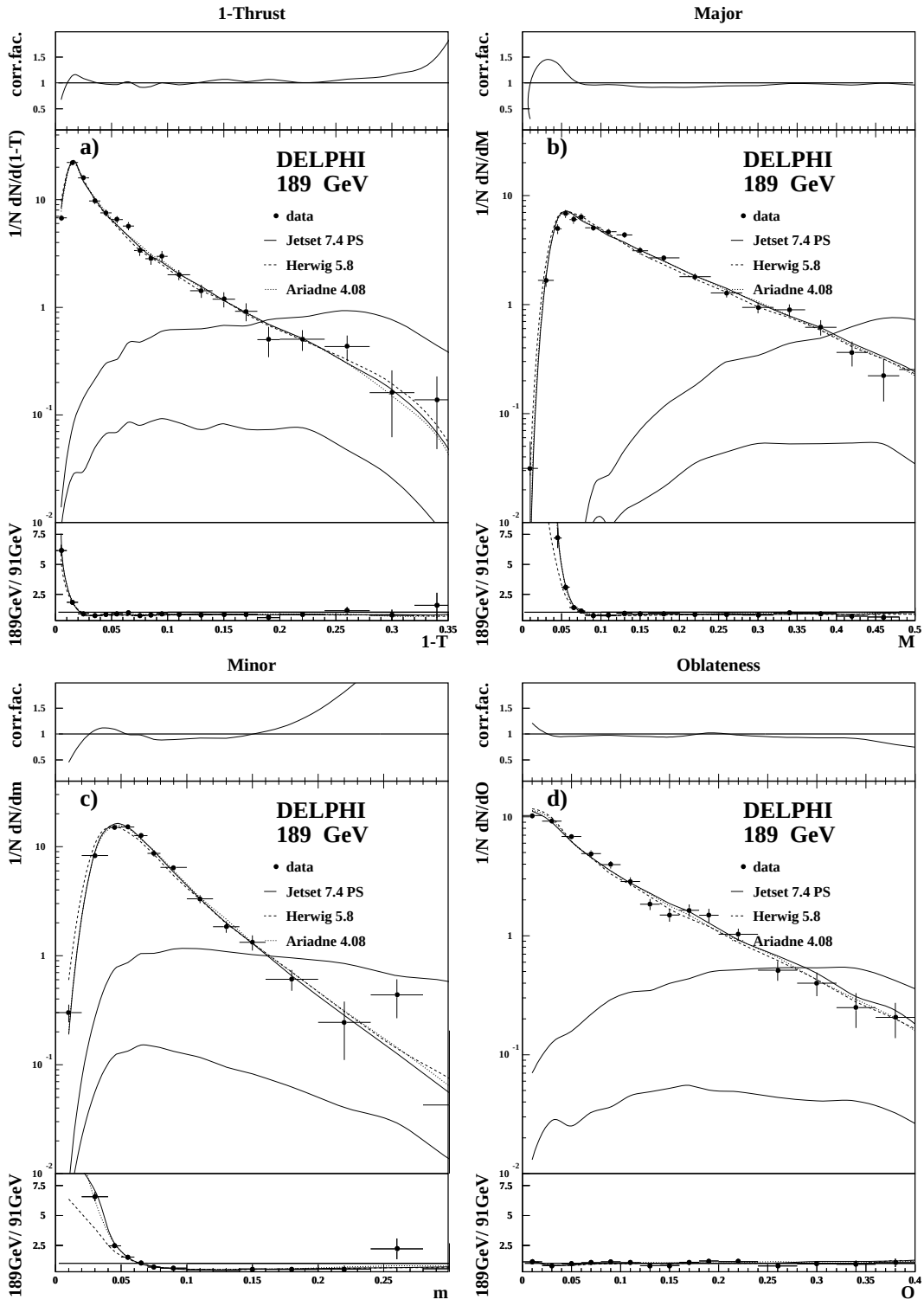

Figure 2: Event shape distributions of Thrust (T), Major (M), Minor (m), and Oblateness (O) at 189 GeV. The upper inset shows the acceptance correction. The middle part shows data, simulation, WW and ZZ background. The lower part shows the ratio of 189 GeV and Z data, again compared to model predictions.

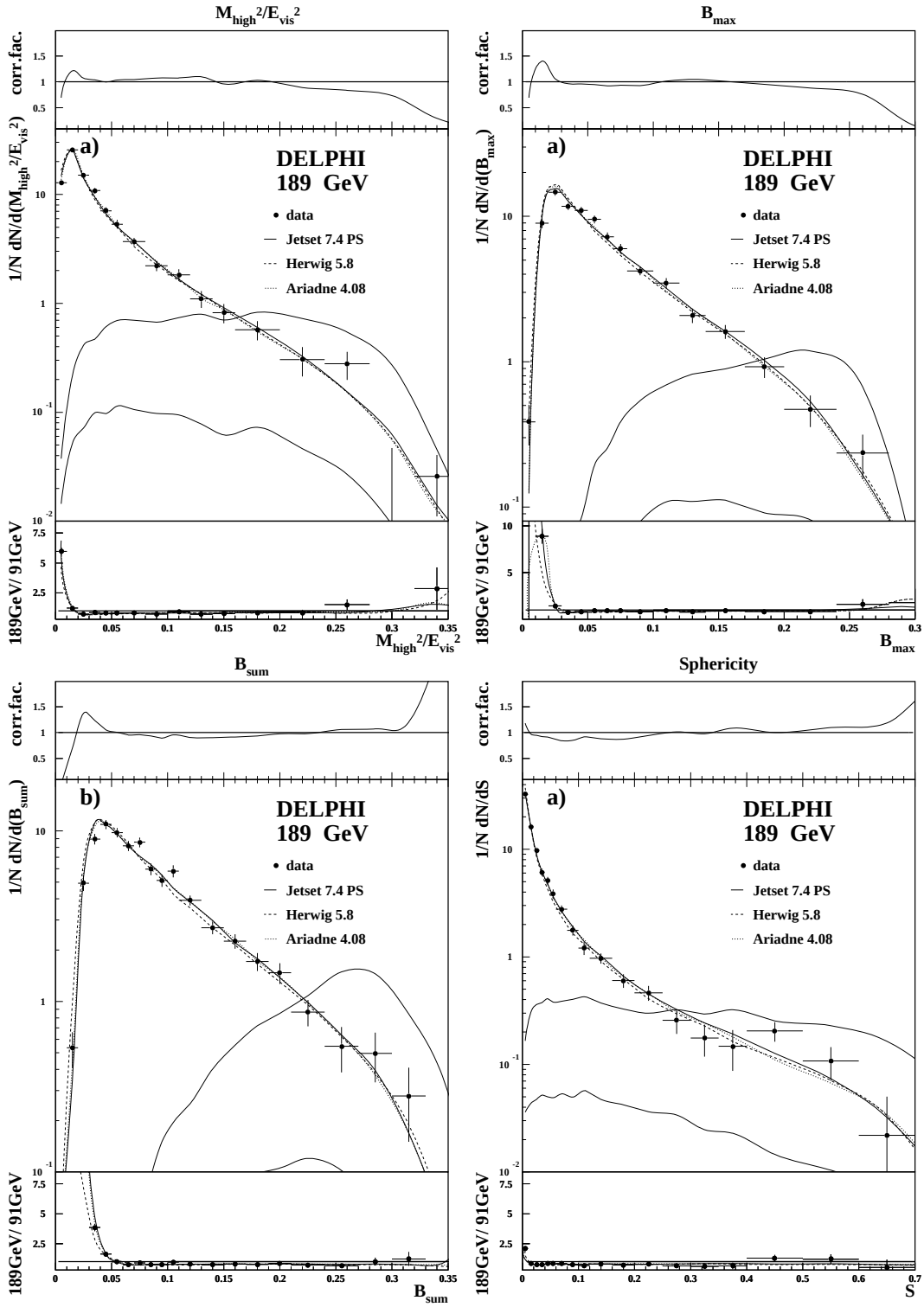

Figure 3: Event shape distributions of Heavy Jetmass ($M_{\mathrm{h}}^2/E_{\mathrm{vis}}^2$), Wide Jet Broadening ($B_{\mathrm{max}}$), Total Jet Broadening (B_{max}), and Sphericity at 189 GeV. The upper inset shows the acceptance correction. The middle part shows data, simulation, WW and ZZ background. The lower part shows the ratio of 189 GeV and Z data, again compared to model predictions.

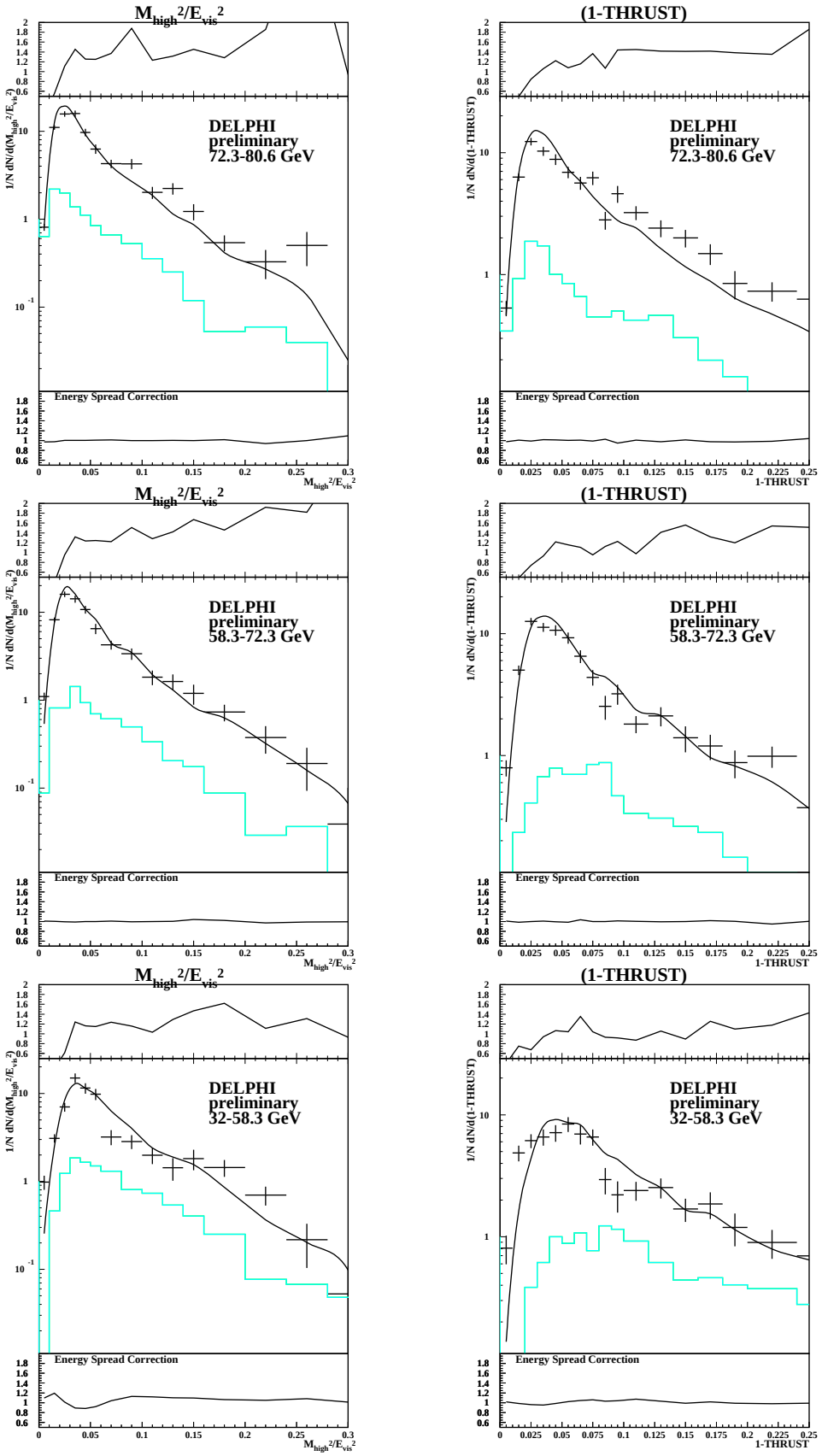

Figure 4: Event shape distributions of Thrust (T) and Heavy Jetmass ($M_{\mathrm{h}}^2/E_{\mathrm{vis}}^2$), at 76, 65 and 41 GeV. The upper inset shows the acceptance correction. The middle part shows data, simulation and nonradiative background. The lower part shows the correction for the energy spread.

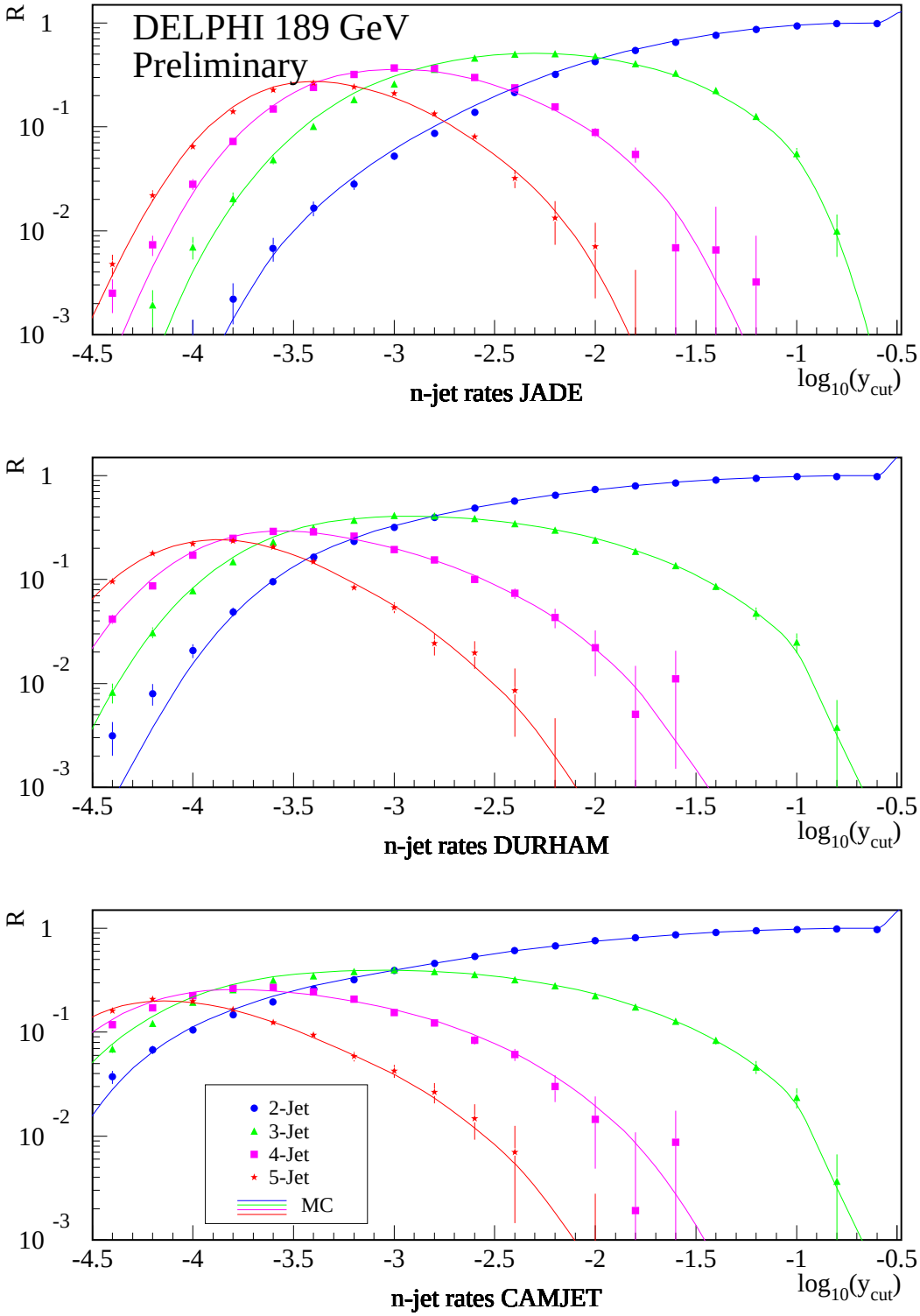

Figure 5: QCD jet rates (R) as a function of y_{cut} compared to the prediction of JETSET7.4 PS

to determine α_s from mean event shapes. This ansatz provides an additive term to the perturbative $\mathcal{O}(\alpha_s^2)$ QCD prediction.

$$\langle f \rangle = \frac{1}{\sigma_{\mathrm{tot}}} \int f \frac{df}{d\sigma} d\sigma = \langle f_{\mathrm{pert}} \rangle + \langle f_{\mathrm{pow}} \rangle \tag{2}$$

where the second order perturbative prediction can be written as

$$\langle f_{\mathrm{pert}} \rangle = A \frac{\alpha_s(\mu)}{2\pi} + \left(A \cdot 2\pi b_0 \ln \frac{\mu^2}{E_{\mathrm{cm}}^2} + B \right) \left(\frac{\alpha_s(\mu)}{2\pi} \right)^2, \tag{3}$$

with A and B being known numbers [14, 15], μ being the renormalisation scale and $b_0 = (33 - 2N_f)/12\pi$. The power correction is given by

$$\langle f_{pow} \rangle = c_f \frac{4C_F}{\pi^2} \mathcal{M} \frac{\mu_I}{E_{\mathrm{cm}}} \left[\alpha_0(\mu_I) - \alpha_s(\mu) - \left(b_0 \cdot \ln \frac{\mu^2}{\mu_I^2} + \frac{K}{2\pi} + 2b_0 \right) \alpha_s^2(\mu) \right] \tag{4}$$

where α_0 is a non-perturbative parameter accounting for the contributions to the event shape below an infrared matching scale μ_I, $K = (67/18 - \pi^2/6)C_A - 5N_f/9$. The Milan factor $\mathcal{M}$ is set to 1.8, which corresponds to three active flavours in the non-perturbative region. The observable-dependent constant c_f is 2 and 1 for $f = \langle 1 - T \rangle$ and $f = \langle M_{\mathrm{h}}^2 / E_{\mathrm{vis}}^2 \rangle$, respectively. In the case of $f = \langle B_{max} \rangle$ c_f cannot be described as a constant. Recent calculations [16] have shown, that for the B observables the non-perturbative contribution becomes proportional to $1/(Q\sqrt{\alpha_s(Q)})$:

$$c_f = \frac{1}{2} \left(\frac{\pi}{2\sqrt{2C_F \alpha_{CMW}(Qe^{-3/4})}} + \frac{3}{4} - \frac{\beta_0}{12C_F} + \eta_0 \right) \tag{5}$$

Where $\eta_0 = -0.6137056$, and α_{CMW} is α_s in the CMW renormalization scheme, which is linked to the $\overline{MS}$ Scheme by:

$$\alpha_{CMW} = \alpha_{\overline{MS}} \left(1 + K \frac{\alpha_{\overline{MS}}}{2\pi} \right) \tag{6}$$

The infrared matching scale is set to 2 GeV as suggested by the authors [10], the renormalization scale μ is set to be equal to E_{cm}. Beside α_s these formulae contain α_0 as the only free parameter. In order to measure α_s from individual high energy data this parameter has to be known.

To infer α_0, a combined fit of α_s and α_0 to a large set of measurements at different energies [17] is performed. For $E_{\mathrm{cm}} \geq M_{\mathrm{Z}}$ only DELPHI measurements are included in the fit. Figure 6 shows the measured mean values of $\langle 1 - T \rangle$, $\langle M_{\mathrm{h}}^2 / E_{\mathrm{vis}}^2 \rangle$ and $\langle B_{\mathrm{max}} \rangle$ as a function of the centre-of-mass energy together with the results of the fit. The resulting values of α_0 are summarized in Table 5. The extracted α_0 values are around 0.5 as expected in [11, 13] within an uncertainty of 20%. α_0 is determined individually for the observables. The scale error is obtained by varying the renormalization scale $x_\mu = \mu^2/E_{\mathrm{cm}}^2$ from 0.25 to 4.

After having fixed α_0, the α_s values corresponding for the DELPHI data points can be calculated from Eqs. (2–4). α_s is calculated for the observables individually and then combined with an unweighted average. Its error is propagated from the data and combined

Observable	$\alpha_0(2\,\mathrm{GeV})$	$\alpha_s(M_\mathrm{Z})$	$\Lambda_{\overline{MS}}$ MeV	χ^2/ndf
$\langle 1-T\rangle$	$0.493 \pm 0.009 \pm 0.006$	$0.119 \pm 0.0014 \pm 0.0067$	$240 \pm 20 \pm 86$	64.0/32
$\langle M_\mathrm{h}^2/E_\mathrm{vis}^2\rangle$	$0.545 \pm 0.023 \pm 0.017$	$0.120 \pm 0.0020 \pm 0.0050$	$246 \pm 27 \pm 67$	8.28/21
$\langle B_{max}\rangle$	$0.407 \pm 0.022 \pm 0.055$	$0.117 \pm 0.0012 \pm 0.0015$	$215 \pm 15 \pm 18$	24.1/17

Table 5: Determination of α_0 from a combined fit of α_0 and α_s to a large set of measurements of different experiments [17]. For $E_\mathrm{cm} \geq M_\mathrm{Z}$ only DELPHI measurements are included in the fit. The first error is the statistical error from the fit, the second one is the scale error.

by assuming maximal correlation. An additional scale error is calculated by varying x_μ and μ_I in the ranges discussed and the infrared matching scale from 1 GeV to 3 GeV. The results are summarized in Table 6 and plotted as function of E_cm together with the QCD expectation in Figure 8.

Its systematic error is obtained by raising/lowering the fitted α_s values by their systematic error contribution due to ISR and WW. All other systematics present in the α_s results are considered to be fully correlated, thus not contributing to the systematic error of the slope. The result agrees with the QCD expectation of a running α_s (Table 7).

5.2 α_s from Event Shape Distributions

From event shape distributions, α_s is determined by fitting an α_s dependent QCD prediction folded with a hadronization correction to the data. As QCD predictions $\mathcal{O}(\alpha_s^2)$, pure NLLA, and the combined $\mathcal{O}(\alpha_s^2)$+NLLA calculations in $\ln R$-scheme are employed [14, 18, 19]. The Hadronization correction is calculated using the JETSET PS model (Version 7.4 as tuned by DELPHI [7]). The QCD prediction is multiplied in each bin by the Hadronization correction

$$C_\mathrm{had}(E_\mathrm{cm}) = \frac{f_\mathrm{had}^\mathrm{Sim.}(E_\mathrm{cm})}{f_\mathrm{part}^\mathrm{Sim.}(E_\mathrm{cm})} \quad , \tag{7}$$

where $f_\mathrm{had}^\mathrm{Sim.}(E_\mathrm{cm})$ ($f_\mathrm{part}^\mathrm{Sim.}(E_\mathrm{cm})$) is the model prediction on hadron (parton) level at the centre-of-mass energy E_cm. The parton level is defined as the final state of the parton shower created by the simulation.

The fit ranges used for the different QCD predictions are shown in Figure 7. The upper limit of the range used for $\mathcal{O}(\alpha_s^2)$+NLLA is reduced with respect to previous publications [20, 21] in order to reduce the systematic uncertainties due to WW background. The lower limit is chosen such that the χ^2/ndf of the QCD fit were reasonable at 189 GeV while maintaining the results at the Z-peak stable. The ranges for pure NLLA and $\mathcal{O}(\alpha_s^2)$ fits are chosen to be distinct, so that the results are statistically uncorrelated. Their limit is taken from [22], where the size of hadronization correction, the size of the B-coefficient, and the stability under fit range changes is considered.

In [22] it has been shown that fixing the renormalization scale to $\mu^2 = E_\mathrm{cm}^2$ results in a marginal description of the data. Therefore, the experimentally optimized scales $x_\mu = \mu^2/E_\mathrm{cm}^2$ are determined from the LEP1 data and are used for the $\mathcal{O}(\alpha_s^2)$ fits to

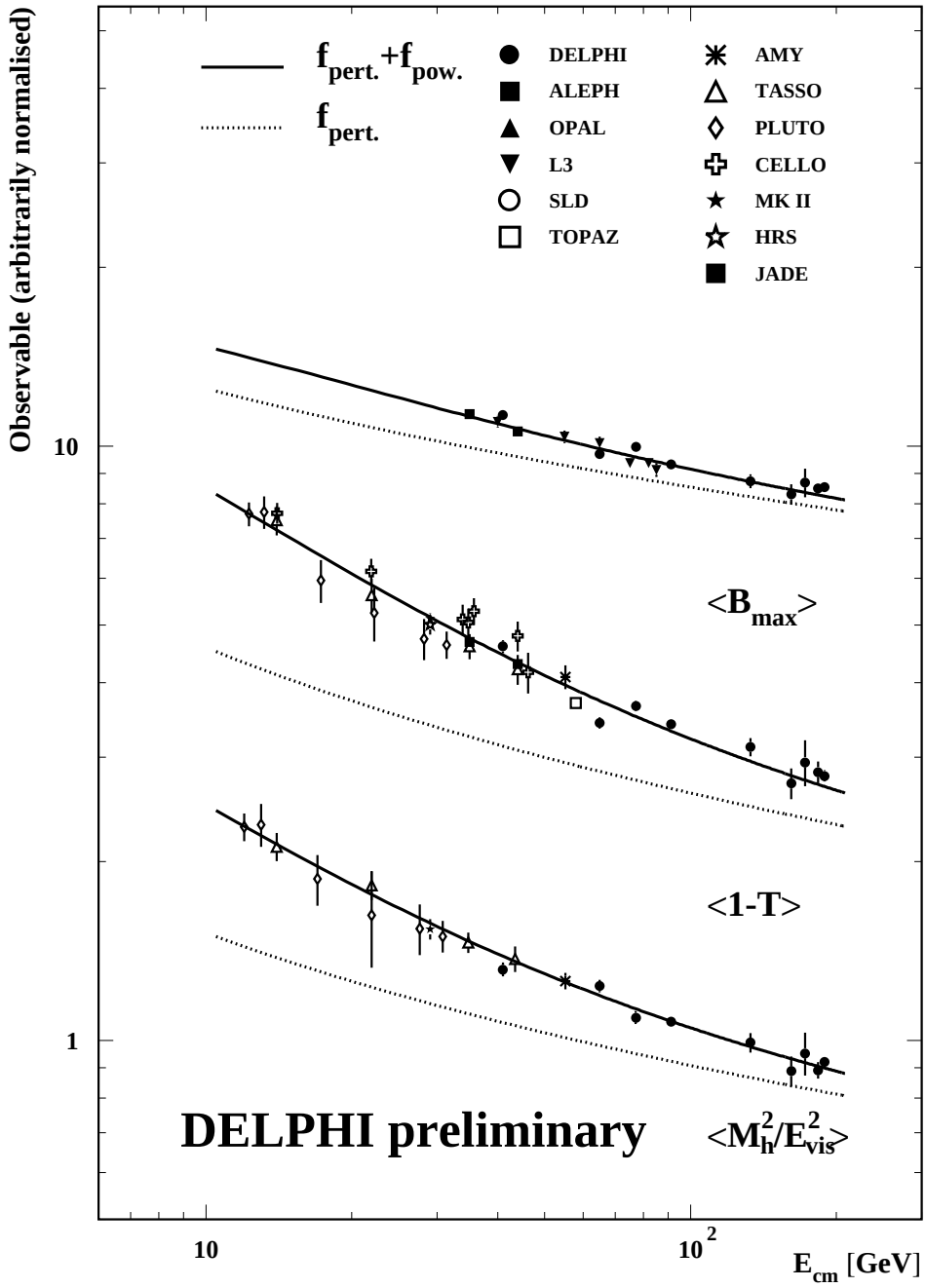

Figure 6: Measured mean values of $\langle 1-T\rangle$, $\langle M_{\rm h}^2/E_{\rm vis}^2\rangle$ and $\langle B_{max}\rangle$ as a function of the centre-of-mass energy. The solid lines present the results of the fits with Eqs. (2–4), the dotted lines show the perturbative part only.

$E_{\rm cm}$	QCD-parameter	Result $\pm$ stat $\pm$ syst $\pm$ scale
41 GeV	$\alpha_s(48\,\text{GeV})$	$0.1381 \pm 0.0066 \pm 0.0049 \pm 0.0028$
	$\alpha_s(M_{\rm Z})$	$0.121 \pm 0.005 \pm 0.0037 \pm 0.0022$
65 GeV	$\alpha_s(66\,\text{GeV})$	$0.1211 \pm 0.0035 \pm 0.0024 \pm 0.0038$
	$\alpha_s(M_{\rm Z})$	$0.1151 \pm 0.0032 \pm 0.0021 \pm 0.0033$
77 GeV	$\alpha_s(76\,\text{GeV})$	$0.1245 \pm 0.0032 \pm 0.0023 \pm 0.0028$
	$\alpha_s(M_{\rm Z})$	$0.1212 \pm 0.0031 \pm 0.0022 \pm 0.0027$
91.2 GeV	$\alpha_s(M_{\rm Z})$	$0.1199 \pm 0.0003 \pm 0.0027 \pm 0.0030$
133 GeV	$\alpha_s(133\,\text{GeV})$	$0.115 \pm 0.0042 \pm 0.0009 \pm 0.0028$
	$\alpha_s(M_{\rm Z})$	$0.1218 \pm 0.0047 \pm 0.0010 \pm 0.0031$
161 GeV	$\alpha_s(161\,\text{GeV})$	$0.1051 \pm 0.0068 \pm 0.0038 \pm 0.0022$
	$\alpha_s(M_{\rm Z})$	$0.1139 \pm 0.0080 \pm 0.0045 \pm 0.0026$
172 GeV	$\alpha_s(172\,\text{GeV})$	$0.1136 \pm 0.0084 \pm 0.0011 \pm 0.0027$
	$\alpha_s(M_{\rm Z})$	$0.1251 \pm 0.0102 \pm 0.0014 \pm 0.0033$
183 GeV	$\alpha_s(183\,\text{GeV})$	$0.1112 \pm 0.0064 \pm 0.0032 \pm 0.0025$
	$\alpha_s(M_{\rm Z})$	$0.1235 \pm 0.0078 \pm 0.0040 \pm 0.0030$
189 GeV	$\alpha_s(189\,\text{GeV})$	$0.1102 \pm 0.0023 \pm 0.0018 \pm 0.0024$
	$\alpha_s(M_{\rm Z})$	$0.1229 \pm 0.0028 \pm 0.0022 \pm 0.0031$

Table 6: α_s as obtained with the Dokshitzer and Webber ansatz by averaging the $\langle 1-T\rangle$, $\langle M_{\rm h}^2/E_{\rm vis}^2\rangle$ and $\langle B_{\rm max}\rangle$ results.

the data for both observables individually. In contrast to the NLLA and the combined NLLA+$\mathcal{O}(\alpha_s^2)$ fits, μ is set equal to $E_{\rm cm}$, in order to compare these results with other experiments more directly.

The systematic errors are obtained from fits to $1-T$ and $M_{\rm h}^2/E_{\rm vis}^2$ distributions evaluated with different cuts using the same variations as for the error determination of the moments. The scale errors for the NLLA and $\mathcal{O}(\alpha_s^2)$+NLLA analysis are calculated by varying x_μ from 0.25 to 4. The scale errors for $\mathcal{O}(\alpha_s^2)$ are taken from a previous DELPHI publication [20]. An error from the influence of the used hadronisation model is estimated by calculating $C_{\rm had}$ (see Eq. 1) with JETSET and ARIADNE. The resulting two values of α_s are averaged to get the central value, half of their difference is added in quadrature to

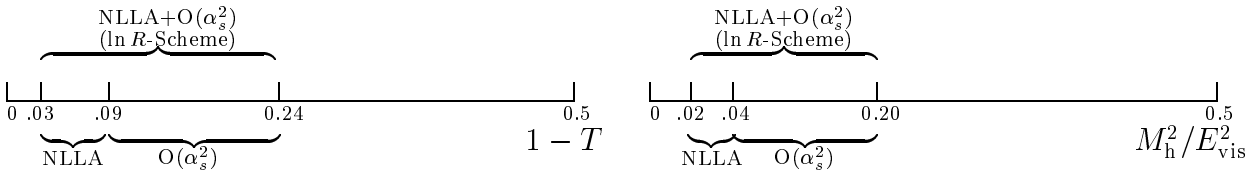

Figure 7: Fit ranges chosen for fitting α_s from different QCD predictions of $1-T$ and $M_{\rm h}^2/E_{\rm vis}^2$ distribution.

Theory used for measurement	$d\alpha_s^{-1}/d\log(E_{\rm cm})$
$\mathcal{O}(\alpha_s^2)$+ power ansatz	1.07 ± 0.19
$\mathcal{O}(\alpha_s^2)$	1.23 ± 0.31
NLLA	1.41 ± 0.31
$\mathcal{O}(\alpha_s^2)$+NLLA ($\ln R$-scheme)	1.12 ± 0.22
QCD expectation	1.27
QCD+Gluinos expectation	0.90

Table 7: Results of straight line fit to the logarithmic energy dependence of α_s^{-1}, and theoretical expectations calculated in 2nd order.

the systematic error.

The α_s values evaluated from the distributions are given in Table 10 and plotted in Figure 8. The results agree within the errors with those measured from the event shape means. Comparing the results with a precision measurement derived from DELPHI Z Data [22], the results are in very good agreement for the $\mathcal{O}(\alpha_s^2)$ results, while the results for NLLA and matched calculations deviate. This is due to the fact, that the analysis in [22] is based on six observables instead of the two in this analysis, and that the fit ranges for the NLLA measurements in this analysis have been optimized for the larger statistical errors of the high energy data.

Starting from the renormalization group equation:

$$E_{cm}^2 \frac{\partial \alpha_s}{\partial E_{cm}^2} = \beta(\alpha_s) = -b_0 \alpha_s^2 (1 + b_1 \alpha_s + \ldots),$$

an equation suited for fitting the slope of the logarithmic energy dependence is obtained:

$$\frac{d\alpha_s^{-1}}{d\log(E_{cm})} = 2b_0 \left(1 + b_1 \alpha_s + \ldots\right),$$

with $b_1 = (153 - 19N_f)/2\pi(33 - 2n_f)$

. Evaluating the equation in full second order with $E_{cm} = 135GeV, \Lambda = 200MeV$ and $N_f = 5$ yields $d\alpha_s^{-1}/d\log E_{cm} = 1.27$.

Thus in leading order this quantity is independent of α_s and E_{cm} and the coefficient b_0 of the β function is measured. The values obtained are in good agreement with the QCD expectation (Table 7).

6 Summary

A measurement of event shape distributions and their moments is presented as obtained from data measured at 189 GeV centre-of-mass energy. The results are compared to previous measurements at centre-of-mass energies between 133 GeV and 183 GeV and to low energy data between 41 GeV and 77 GeV, reconstructed by tagging radiative events. The measurement of event shape distributions and their moments is presented as obtained

from data measured at 189 GeV centre-of-mass energy and compared to previous measurements at centre-of-mass energies between 133 GeV and 183 GeV. The observed jet rates give no indication for an excess of multi-jet events at high energies.

The strong coupling α_s has been determined from the means and the distributions of $1-T$, $M_{\mathrm{h}}^2/E_{\mathrm{vis}}^2$ and $B_{\max}$ using $\mathcal{O}(\alpha_s^2)$, NLLA, and combined QCD predictions (see Table 10 and 6).

Non-perturbative corrections to the shape means were based on their energy evolution using a power correction ansatz. For the shape distributions these non-perturbative corrections were performed directly by applying analytical corrections, and using the fragmentation models JETSET and ARIADNE. Within the large statistical errors the different methods yield consistent results.

The comparison of α_s as measured at the Z and at higher energies confirms that the energy dependence (running) of the strong coupling is consistent with QCD expectation. It is measured to be

$$\frac{d\alpha_s^{-1}}{d\log(E_{cm})} = 1.12 \pm 0.22(stat)$$

.

$E_{\rm cm}$	Mean	2nd Moment	3rd Moment
	$< 1-T >$		
41 GeV	0.0921 $\pm$ 0.0023 $\pm$ 0.0027	0.0014 $\pm$ 0.0008 $\pm$ 0.0008	0.00263 $\pm$ 0.00023 $\pm$ 0.00025
65 GeV	0.0685 $\pm$ 0.0015 $\pm$ 0.0012	0.0089 $\pm$ 0.0005 $\pm$ 0.0003	0.00166 $\pm$ 0.00014 $\pm$ 0.00009
77 GeV	0.0731 $\pm$ 0.0015 $\pm$ 0.0014	0.0100 $\pm$ 0.0005 $\pm$ 0.0004	0.00189 $\pm$ 0.00016 $\pm$ 0.00010
91.2 GeV	0.06823 $\pm$ 0.00006 $\pm$ 0.00065	0.00837 $\pm$ 0.00002 $\pm$ 0.00009	0.001504 $\pm$ 0.000004 $\pm$ 0.000016
133 GeV	0.0624 $\pm$ 0.0022 $\pm$ 0.0005	0.0078 $\pm$ 0.0006 $\pm$ 0.0001	0.00144 $\pm$ 0.00015 $\pm$ 0.00006
161 GeV	0.0542 $\pm$ 0.0031 $\pm$ 0.0025	0.0058 $\pm$ 0.0008 $\pm$ 0.0003	0.00092 $\pm$ 0.00019 $\pm$ 0.00005
172 GeV	0.0588 $\pm$ 0.0052 $\pm$ 0.0011	0.0071 $\pm$ 0.0015 $\pm$ 0.0005	0.00124 $\pm$ 0.00046 $\pm$ 0.00020
183 GeV	0.0575 $\pm$ 0.0033 $\pm$ 0.0016	0.0068 $\pm$ 0.0011 $\pm$ 0.0004	0.00118 $\pm$ 0.00038 $\pm$ 0.00011
189 GeV	0.0558 $\pm$ 0.0012 $\pm$ 0.0017	0.0065 $\pm$ 0.0004 $\pm$ 0.0006	0.00111 $\pm$ 0.00014 $\pm$ 0.00019
	$< B_{\rm max} >$		
41 GeV	0.0902 $\pm$ 0.0017 $\pm$ 0.0018	0.0124 $\pm$ 0.0005 $\pm$ 0.0005	0.00194 $\pm$ 0.00011 $\pm$ 0.00012
65 GeV	0.0775 $\pm$ 0.0011 $\pm$ 0.0010	0.0084 $\pm$ 0.0003 $\pm$ 0.0003	0.00118 $\pm$ 0.00007 $\pm$ 0.00007
77 GeV	0.0798 $\pm$ 0.0010 $\pm$ 0.0010	0.0089 $\pm$ 0.0002 $\pm$ 0.0002	0.00126 $\pm$ 0.00006 $\pm$ 0.00006
91.2 GeV	0.07442 $\pm$ 0.00006 $\pm$ 0.00046	0.00782 $\pm$ 0.00001 $\pm$ 0.00007	0.001069 $\pm$ 0.000002 $\pm$ 0.000010
133 GeV	0.0699 $\pm$ 0.0018 $\pm$ 0.0008	0.0075 $\pm$ 0.0005 $\pm$ 0.0002	0.00108 $\pm$ 0.00010 $\pm$ 0.00003
161 GeV	0.0664 $\pm$ 0.0026 $\pm$ 0.0019	0.0064 $\pm$ 0.0006 $\pm$ 0.0003	0.00082 $\pm$ 0.00018 $\pm$ 0.00003
172 GeV	0.0695 $\pm$ 0.0039 $\pm$ 0.0008	0.0075 $\pm$ 0.0007 $\pm$ 0.0002	0.00109 $\pm$ 0.00010 $\pm$ 0.00003
183 GeV	0.0675 $\pm$ 0.0020 $\pm$ 0.0016	0.0070 $\pm$ 0.0005 $\pm$ 0.0003	0.00095 $\pm$ 0.00009 $\pm$ 0.00006
189 GeV	0.0683 $\pm$ 0.0007 $\pm$ 0.0009	0.0073 $\pm$ 0.0002 $\pm$ 0.0002	0.00105 $\pm$ 0.00004 $\pm$ 0.00006

Table 8: Event shape means and higher moments for $1-T$ and $B_{\rm max}$. The first error is statistical, the second systematic.

$E_{\rm cm}$	Mean	2nd Moment	3rd Moment
	$< M_{\rm h}^2/E_{\rm vis}^2 >$		
41 GeV	0.0659 ± 0.0018 ± 0.0017	0.0079 ± 0.0005 ± 0.0005	0.00139 ± 0.00018 ± 0.00018
65 GeV	0.0618 ± 0.0015 ± 0.0012	0.0051 ± 0.0003 ± 0.0002	0.00079 ± 0.00009 ± 0.00005
77 GeV	0.0547 ± 0.0014 ± 0.0014	0.0059 ± 0.0004 ± 0.0003	0.00094 ± 0.00012 ± 0.00008
91.2 GeV	0.05383 ± 0.00005 ± 0.00073	0.00524 ± 0.00001 ± 0.00007	0.000761 ± 0.000002 ± 0.000007
133 GeV	0.0496 ± 0.0026 ± 0.0004	0.0053 ± 0.0005 ± 0.0001	0.00087 ± 0.00012 ± 0.00003
161 GeV	0.0444 ± 0.0039 ± 0.0023	0.0040 ± 0.0009 ± 0.0004	0.00056 ± 0.00013 ± 0.00012
172 GeV	0.0476 ± 0.0020 ± 0.0005	0.0050 ± 0.0005 ± 0.0001	0.00080 ± 0.00023 ± 0.00002
183 GeV	0.0456 ± 0.0017 ± 0.0015	0.0043 ± 0.0004 ± 0.0004	0.00063 ± 0.00011 ± 0.00007
189 GeV	0.0460 ± 0.0008 ± 0.0010	0.0047 ± 0.0002 ± 0.0003	0.00077 ± 0.00005 ± 0.00007
	$< y_{32}^{k_\perp} >$		
41 GeV	0.0306 ± 0.0028 ± 0.0025	0.0033 ± 0.0008 ± 0.0007	0.00050 ± 0.00019 ± 0.00017
65 GeV	0.0216 ± 0.0015 ± 0.001	0.0023 ± 0.0004 ± 0.0003	0.00032 ± 0.00010 ± 0.00007
77 GeV	0.0211 ± 0.0018 ± 0.001	0.0032 ± 0.0004 ± 0.0004	0.00048 ± 0.00009 ± 0.00008
91.2 GeV	0.02090 ± 0.00004 ± 0.00020	0.00197 ± 0.00001 ± 0.00004	0.000305 ± 0.000002 ± 0.000009
133 GeV	0.0220 ± 0.0018 ± 0.0002	0.0025 ± 0.0004 ± 0.0001	0.00046 ± 0.00012 ± 0.00002
161 GeV	0.0184 ± 0.0031 ± 0.0012	0.0020 ± 0.0009 ± 0.0003	0.00042 ± 0.00025 ± 0.00010
172 GeV	0.0225 ± 0.0040 ± 0.0015	0.0028 ± 0.0010 ± 0.0007	0.00057 ± 0.00028 ± 0.00022
183 GeV	0.0187 ± 0.0019 ± 0.0009	0.0016 ± 0.0004 ± 0.0001	0.00024 ± 0.00011 ± 0.00003
189 GeV	0.0195 ± 0.0009 ± 0.0011	0.0019 ± 0.0002 ± 0.0003	0.00030 ± 0.00005 ± 0.00006

Table 9: Event shape means and higher moments for $M_{\rm h}^2/E_{\rm vis}^2$ and $y_{32}^{k_\perp}$. The first error is statistical, the second systematic.

$E_{\rm cm}$	Theory	QCD-parameter	Result $\pm$ stat $\pm$ sys $\pm$ scale
76 GeV	$\mathcal{O}(\alpha_s^2)$	$\alpha_s(76\,\text{GeV})$	0.122 $\pm$ 0.0055 $\pm$ $\pm$
		$\alpha_s(M_{\rm Z})$	0.1186 $\pm$ 0.0052 $\pm$ $\pm$
	NLLA	$\alpha_s(76\,\text{GeV})$	0.1232 $\pm$ 0.0072 $\pm$ $\pm$
		$\alpha_s(M_{\rm Z})$	0.1197 $\pm$ 0.0067 $\pm$ $\pm$
	$\mathcal{O}(\alpha_s^2)$+NLLA	$\alpha_s(76\,\text{GeV})$	0.1266 $\pm$ 0.0044 $\pm$ $\pm$
	($\ln R$-scheme)	$\alpha_s(M_{\rm Z})$	0.1229 $\pm$ 0.0041 $\pm$ $\pm$
91.2 GeV	$\mathcal{O}(\alpha_s^2)$	$\alpha_s(M_{\rm Z})$	0.1186 $\pm$ 0.0002 $\pm$ 0.0015 $\pm$ 0.006
	NLLA	$\alpha_s(M_{\rm Z})$	0.1221 $\pm$ 0.0002 $\pm$ 0.0039 $\pm$ 0.0087
	$\mathcal{O}(\alpha_s^2)$+NLLA	$\alpha_s(M_{\rm Z})$	0.1246 $\pm$ 0.0002 $\pm$ 0.0024 $\pm$ 0.0063
133 GeV	$\mathcal{O}(\alpha_s^2)$	$\alpha_s(133\,\text{GeV})$	0.1097 $\pm$ 0.0046 $\pm$ 0.0009 $\pm$ 0.005
		$\alpha_s(M_{\rm Z})$	0.1158 $\pm$ 0.0052 $\pm$ 0.0010 $\pm$ 0.006
	NLLA	$\alpha_s(133\,\text{GeV})$	0.1104 $\pm$ 0.0074 $\pm$ 0.0020 $\pm$ 0.0057
		$\alpha_s(M_{\rm Z})$	0.1166 $\pm$ 0.0082 $\pm$ 0.0023 $\pm$ 0.0064
	$\mathcal{O}(\alpha_s^2)$+NLLA	$\alpha_s(133\,\text{GeV})$	0.1136 $\pm$ 0.0043 $\pm$ 0.0013 $\pm$ 0.0048
	($\ln R$-scheme)	$\alpha_s(M_{\rm Z})$	0.1202 $\pm$ 0.0048 $\pm$ 0.0014 $\pm$ 0.0053
161 GeV	$\mathcal{O}(\alpha_s^2)$	$\alpha_s(161\,\text{GeV})$	0.1085 $\pm$ 0.0076 $\pm$ 0.0011 $\pm$ 0.005
		$\alpha_s(M_{\rm Z})$	0.1178 $\pm$ 0.0091 $\pm$ 0.0012 $\pm$ 0.006
	NLLA	$\alpha_s(161\,\text{GeV})$	0.1059 $\pm$ 0.0104 $\pm$ 0.0015 $\pm$ 0.0046
		$\alpha_s(M_{\rm Z})$	0.1147 $\pm$ 0.0123 $\pm$ 0.0018 $\pm$ 0.0054
	$\mathcal{O}(\alpha_s^2)$+NLLA	$\alpha_s(161\,\text{GeV})$	0.1131 $\pm$ 0.0068 $\pm$ 0.0021 $\pm$ 0.0046
	($\ln R$-scheme)	$\alpha_s(M_{\rm Z})$	0.1232 $\pm$ 0.0080 $\pm$ 0.0026 $\pm$ 0.0055

Table 10: α_s as obtained from distributions by averaging the results from the $1-T$ and $M_{\rm h}^2/E_{\rm vis}^2$. The scale errors for the $\mathcal{O}(\alpha_s^2)$ analysis are taken from a previous DELPHI publication [20]. The results for 76 GeVare preliminary. The estimation of systematic errors is not finished yet.

$E_{\rm cm}$	Theory	QCD-parameter	Result $\pm$ stat $\pm$ sys $\pm$ scale
172 GeV	$\mathcal{O}(\alpha_s^2)$	$\alpha_s(172\,\text{GeV})$	$0.1093 \pm 0.0094 \pm 0.0010 \pm 0.005$
		$\alpha_s(M_{\rm Z})$	$0.1199 \pm 0.0113 \pm 0.0012 \pm 0.006$
	NLLA	$\alpha_s(172\,\text{GeV})$	$0.1041 \pm 0.0091 \pm 0.0011 \pm 0.0057$
		$\alpha_s(M_{\rm Z})$	$0.1139 \pm 0.0107 \pm 0.0013 \pm 0.0070$
	$\mathcal{O}(\alpha_s^2)$+NLLA	$\alpha_s(172\,\text{GeV})$	$0.1087 \pm 0.0081 \pm 0.0013 \pm 0.0042$
	($\ln R$-scheme)	$\alpha_s(M_{\rm Z})$	$0.1193 \pm 0.0098 \pm 0.0016 \pm 0.0050$
183 GeV	$\mathcal{O}(\alpha_s^2)$	$\alpha_s(183\,\text{GeV})$	$0.1102 \pm 0.0044 \pm 0.0019 \pm 0.005$
		$\alpha_s(M_{\rm Z})$	$0.1222 \pm 0.0054 \pm 0.0023 \pm 0.006$
	NLLA	$\alpha_s(183\,\text{GeV})$	$0.1094 \pm 0.0055 \pm 0.0028 \pm 0.0056$
		$\alpha_s(M_{\rm Z})$	$0.1212 \pm 0.0068 \pm 0.0034 \pm 0.0070$
	$\mathcal{O}(\alpha_s^2)$+NLLA	$\alpha_s(183\,\text{GeV})$	$0.1132 \pm 0.0038 \pm 0.0013 \pm 0.0049$
	($\ln R$-scheme)	$\alpha_s(M_{\rm Z})$	$0.1259 \pm 0.0048 \pm 0.0016 \pm 0.0061$
189 GeV	$\mathcal{O}(\alpha_s^2)$	$\alpha_s(189\,\text{GeV})$	$0.1065 \pm 0.0034 \pm \quad \pm$
		$\alpha_s(M_{\rm Z})$	$0.1182 \pm 0.0042 \pm \quad \pm$
	NLLA	$\alpha_s(189\,\text{GeV})$	$0.1097 \pm 0.0035 \pm \quad \pm$
		$\alpha_s(M_{\rm Z})$	$0.1222 \pm 0.0044 \pm \quad \pm$
	$\mathcal{O}(\alpha_s^2)$+NLLA	$\alpha_s(189\,\text{GeV})$	$0.1116 \pm 0.0024 \pm \quad \pm$
	($\ln R$-scheme)	$\alpha_s(M_{\rm Z})$	$0.1246 \pm 0.0030 \pm \quad \pm$

Table 11: α_s as obtained from distributions by averaging the results from the $1-T$ and $M_{\rm h}^2/E_{\rm vis}^2$. The scale errors for the $\mathcal{O}(\alpha_s^2)$ analysis are taken from a previous DELPHI publication [20].The results for 189 GeVare preliminary. The estimation of systematic errors is not finished yet.

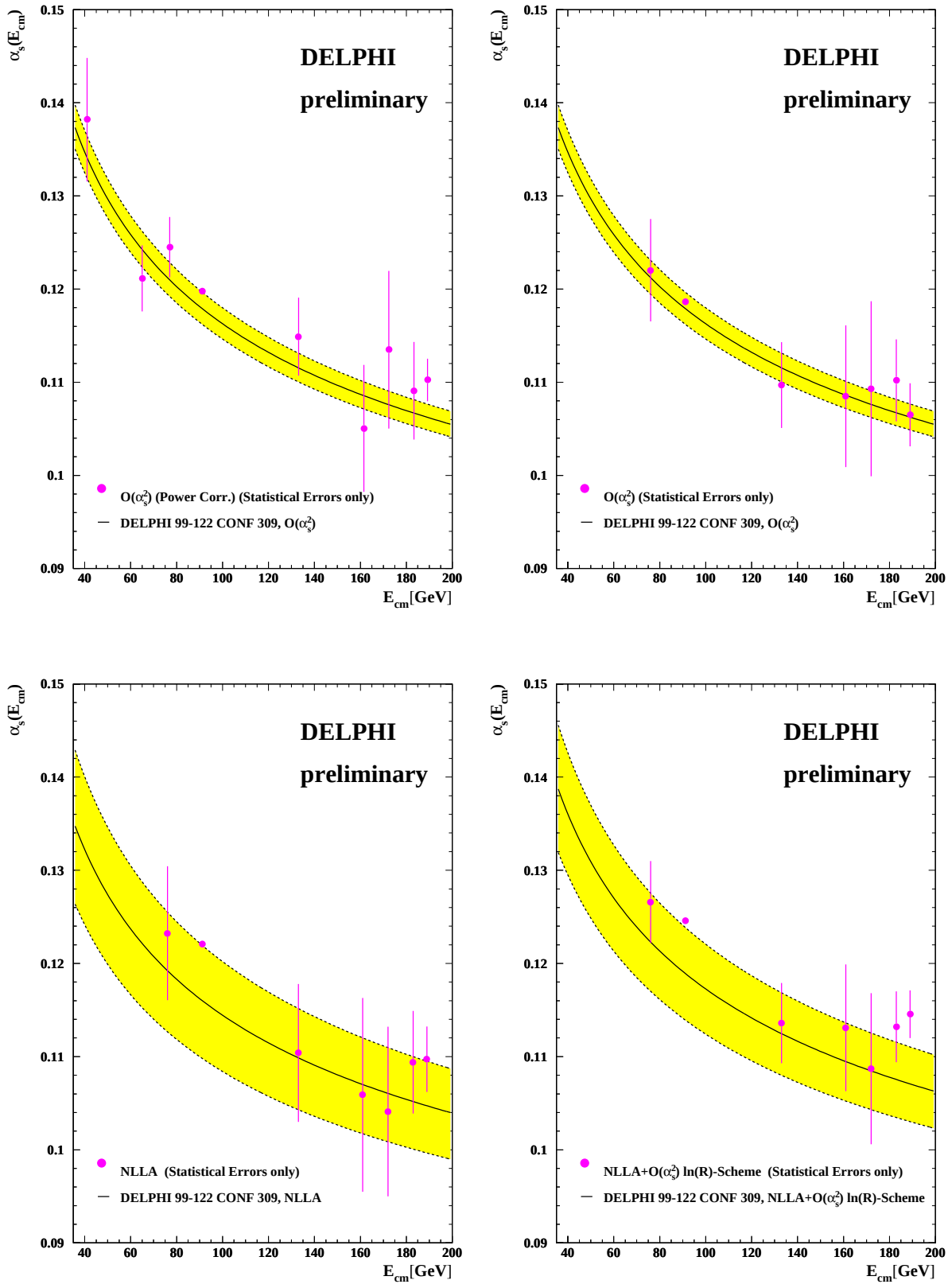

Figure 8: Energy dependence of α_s as obtained from mean event shapes (top left) compared to α_s obtained from distributions. The errors shown are statistical only. The band shows the QCD expectation based on an extended α_s measurement from Z data [22].

References

[1] DELPHI Coll. Energy Dependence of Event Shapes and of alpha s at LEP 2. DELPHI. DELPHI EP210, accepted by Phys. Lett., 1999.

[2] D. Bardin et al. ZFITTER, an analytical program for fermion pair production in e^+e^- annihilation. CERN-TH. 6443/92.

[3] DELPHI Coll., P. Abreu et al. The DELPHI detector at LEP. *Nucl. Instr. Meth.* **A303**(1991) 233.

[4] DELPHI Coll., P. Abreu et al. Performance of the DELPHI detector. *Nucl. Instr. Meth.* **A378**(1996) 57.

[5] P. Abreu, A. De Angelis, G. Della Ricca, D. Fassouliotis, A. Grefrath, N. Kjaer, R. Henriques, M. Mulders, M. Pimenta, and L. Vitale. The estimation of the effective centre of mass energy in $q\bar{q}\gamma$ events from DELPHI. CERN-OPEN 98-026,hep-ex/9809008, accepted by Nucl. Instr. Meth. A.

[6] T. Sjöstrand. *Comp. Phys. Comm.* **39**(1986) 347.

[7] DELPHI Coll., P. Abreu et al. Tuning and test of fragmentation models based on identified particles and precision event shape data. *Z. Phys.* **C73**(1996) 11.

[8] G. Marchesini, B.R. Webber, G. Abbiendi, I.G. Knowles, M.H. Seymour, and L. Stanco. HERWIG. *Computer Phys. Commun.* **67**(1992) 465.

[9] Yu. L. Dokshitzer, G. D. Leder, S. Moretti, and B.R. Webber. Better jet clustering algorithms. Cavendish-HEP-97/06, hep-ph/9707323.

[10] Y. L. Dokshitzer and B. R. Webber. Calculation of power corrections to hadronic event shapes. *Phys. Lett.* **B352**(1995) 451.

[11] B. R. Webber. Hadronic final states. Talk given at workshop on DIS and QCD in Paris, hep-ph/9510283, Apr 1995.

[12] Yu. L. Dokshitzer, A. Lucenti, G. Marchesini, and G. P. Salam. Universality of $1/q$ corrections to jet-shape observables rescued. *Nucl. Phys* **B511**(1997) 396.

[13] Yu. L. Dokshitzer, A. Lucenti, G. Marchesini, and G. P. Salam. On the universality of the Milan factor for $1/Q$ power corrections to jet shapes. hep-ph/9802381, 1998.

[14] R. K. Ellis, D. A. Ross, and A. E. Terrano. *Nucl. Phys* **B178**(1981) 412.

[15] Physics at LEP 1. CERN 89-08 Vol. 1, 1989.

[16] Yu. L. Dokshitzer, G. Marchesini, and G. P. Salam. Revisiting non-pertubative effects in the jet broadenings. hep-ph/9812487, 1998.

[17] ALEPH Coll., D. Decamp et al. *Phys. Lett.* **B284** (1992) 163.
ALEPH Coll., D. Buskulic et al. *Z. Phys.* **C55** (1992) 209.
AMY Coll., I.H. Park et al. *Phys. Rev.* Lett. **62** (1989) 1713.
AMY Coll., Y.K. Li et al. *Phys. Rev.* **D41** (1990) 2675.
CELLO Coll., H.J. Behrend et al. *Z. Phys.* **C44** (1989) 63.
HRS Coll., D. Bender et al. *Phys. Rev.* **D31** (1985) 1.
P.A. Movilla Fernandez, et. al. and the JADE Coll. *Eur. Phys. J.* **C1** (1998) 461.
L3 Coll., B. Adeva et al. *Z. Phys.* **C55** (1992) 39.
Mark II Coll., A. Peterson et al. *Phys. Rev.* **D37** (1988) 1.
Mark II Coll., S. Bethke et al. *Z. Phys.* **C43** (1989) 325.
MARK J Coll., D. P. Barber et al. *Phys. Rev. Lett.* **43** (1979) 831.
OPAL Coll., P. Acton et al. *Z. Phys.* **C59** (1993) 1.
PLUTO Coll., C. Berger et al. *Z. Phys.* **C12** (1982) 297.
SLD Coll., K. Abe et al. *Phys. Rev.* **D51** (1995) 962.
TASSO Coll., W. Braunschweig et al. *Phys.* Lett. **B214** (1988) 293.
TASSO Coll., W. Braunschweig et al. *Z. Phys.* **C45** (1989) 11.
TASSO Coll., W. Braunschweig et al. *Z. Phys.* **C47** (1990) 187.
TOPAZ Coll., I. Adachi et al. *Phys. Lett.* **B227** (1989) 495.
TOPAZ Coll., K. Nagai et al. *Phys. Lett.* **B278** (1992) 506.
TOPAZ Coll., Y. Ohnishi et al. *Phys. Lett.* **B313** (1993) 475. .

[18] S. Catani, G. Turnock, B. R. Webber, and L. Trentadue. Thrust distribution in e^+e^- annihilation. *Phys. Lett.* **B263**(1991) 491.

[19] S. Catani, G. Turnock, and B. R. Webber. Heavy jet mass distribution in e^+e^- annihilation. *Phys. Lett.* **B272**(1991) 368.

[20] DELPHI Coll., P. Abreu et al. Determination of α_s in second order QCD from hadronic z decays. *Z. Phys.* **C54**(1992) 21.

[21] DELPHI Coll., P. Abreu et al. *Z. Phys.* **C59**(1993) 21.

[22] J. Drees S. Hahn and G. Rodrigo. Consistent measurements of α_s from precise oriented event shapes. DELPHI 99-122 CONF 309, 1999.